Article

Journal of
Nanoscience and Nanotechnology
Vol. 17, 6178–6189, 2017
www.aspbs.com/jnn

Nanoscale Pore Characteristics and Influential Factors of Niutitang Formation Shale Reservoir in Guizhou Province

Yuantao Gu[1,2], Quan Wan[1,*], Zonghua Qin[1], Taiyi Luo[1], Shanshan Li[1,2,3], Yuhong Fu[1,2], and Zhongbin Yu[1,2]

[1] *State Key Laboratory of Ore Deposit Geochemistry, Institute of Geochemistry, Chinese Academy of Sciences, Guiyang 550081, Guizhou, China*
[2] *University of Chinese Academy of Sciences, Beijing 100049, China*
[3] *School of Chemistry and Materials Science, Guizhou Normal University, Guiyang 550001, Guizhou, China*

Nanoscale pore characteristics are crucial in assessing the resource potential of gas shales. Although the Niutitang formation was widely deposited in the upper Yantze Platform, South China and has been recognized as a promising shale gas reservoir, there lacks substantial breakthrough in the exploitation of shale gas from the Niutitang formation. Aiming at better understanding the reservoir properties and corresponding influential factors, 14 core samples from the Lower Cambrian Niutitang formation locating in the central Guizhou province were investigated in the current study to characterize the nanoscale pore system in the shale. Organic geochemical analyses (i.e., total organic carbon content and thermal maturity), X-ray diffraction, low pressure nitrogen adsorption, and field emission scanning electron microscopy were employed to obtain complementary information of the pore system. Measured TOC in this study is generally $>$1.50% and averages 3.35%. All of the samples are in the over-maturity stage with R_o ranging from 2.39% to 3.29%. X-ray diffraction shows that quartz, clay minerals and plagioclase are the dominant minerals. Nitrogen adsorption results indicate that all of samples show type IIb nitrogen adsorption isotherms with type H3 hysteresis loops, which imply the coexistence of micropores, mesopores and macropores in the shale. The mesopores account for 60–70% of total pore volume, and are likely contributed by clay minerals and quartz. Organic matter appears to be the major contributor of the micropores and specific surface area, and is closely linked to the rapid decrease of average pore size with increasing burial depth. The field emission scanning electron microscopy reveals abundant organic matter pores in the middle-upper Niutitang formation, but lesser or smaller in the bottom of Niutitang formation. The lower Niutitang formation seems to develop substantial amounts of organic-clay aggregates, which preferentially lie parallel to the shale bedding and contain lots of nanoscale pores. The perpendicular variation of pore structure features is explained with multiple mechanisms, including thermal maturation of organic matter, compaction by strata pressure, dissipation of shale gas, etc. The results of our study have emphasized the interesting and complex features of the nanoscale pore structures in the gas shales, which may facilitate future assessment and exploitation of shale gas resources.

Keywords: Nanoscale Pores, Niutitang Formation, Organic Matter Pores, Organic-Clay Aggregates, Thermal Maturation, Compaction.

1. INTRODUCTION

Shale gas has been successfully exploited in the US and Canada.[1,2] China is estimated to have the largest shale gas reserves in the world. Marine shale, continental shale and marine-terrigenous shale were extensively developed in China, with continental shale and marine-terrigenous shale mostly developed in North China (e.g., Songliao Basin, Bohai Bay Basin, Ordos Basin, Qaidam Basin, etc.) and marine shale widely developed around South China (e.g., Sichuan Basin).[3,4] Yet, shale gas exploration and development in China is still in its infancy with limited success in certain regions such as the Jiaoshiba area in the Sichuan

*Author to whom correspondence should be addressed.

 1533-4880/2017/17/6178/012 doi:10.1166/jnn.2017.14420

Basin.[5–7] The Sichuan Basin is one of the most promising places for shale gas in China.[4] In and around the Sichuan Basin, the Lower Cambrian Niutitang formation ($\in_1$n) and Upper Ordovician Wufeng-Lower Silurian Longmaxi formation (O_3w-S_1l) have been identified as primary shale gas reservoirs.[4] The great potential of O_3w-S_1l shale has been demonstrated by the success in the Jiaoshiba shale gas field, with cumulative production exceeding 60×10^8 m^3 by the end of 2015.[5–7] In contrast, the exploitation of $\in_1$n has not been very successful and so far industrial gas flow has been obtained only in few areas.[6, 8, 9]

Shale gas systems essentially are continuous-type natural gas accumulations characterized by widespread gas saturation, non-obvious trap boundary, and relatively short distances of hydrocarbon migration.[2, 3, 10] Unlike conventional systems, gas shales normally show low porosity (<10%) and low permeability (micro- to nanodarcy range), and serve as sources, reservoirs, and seals for gas accumulations. The characteristics of gas shales are substantially controlled by their composition and pore structures. Strong heterogeneity in shale constituent is thought to result from depositional and diagenetic processes,[10] which may have profound effects on the material basis of hydrocarbon generation. Pore systems in shale gas reservoirs are the main space for the generation, storage, and seepage of shale gas, and previous studies have revealed that the dominant pore size ranges are in the nanometer scale.[1, 11–14] Therefore, the nanoscale pore characteristics of shale gas reservoirs have been established as a key parameter in the evaluation of shale gas resources. Consequently, a great variety of advanced techniques and methods have been utilized to characterize various attributes of nanoscale pores in shale gas reservoirs.[1, 8, 11, 15–19] For example, pore types, shapes and sizes can be directly visualized by utilizing field emission scanning electron microscopy/transmission electron microscopy (FE-SEM/TEM) and focused ion beam scanning electron microscopy (FIB-SEM).[1, 8, 20–23] Specific surface area, pore volume and pore size distribution can be obtained by gas adsorption (low-pressure N_2 adsorption and CO_2 adsorption).[1, 16, 17, 24–26] Alternative approaches, such as mercury injection capillary pressure (MICP), nano X-ray computerized tomography (Nano-CT) and small angle scattering, are also used to study the nanoscale pores in gas shale.[16, 27–29]

Despite a somewhat disappointing exploration of the $\in_1$n shale gas resources, many recent studies have indicated that $\in_1$n actually possesses several traits to be favorable shale gas reservoirs.[3] For example, the shale strata are relatively thick and the principal mineral is quartz;[30–32] the total organic carbon (TOC) content is generally >2% and the organic matter is normally in over-maturation stage;[8, 20, 33] the reservoir porosity ranges from 0.40% to 7.82% and matrix permeability is approximately $1 \times 10^{-5} - 9 \times 10^{-4}$ mD;[5] the reservoir gas-bearing capacity is 0.50–6.02 m^3/t and the average capacity (1.29 m^3/t) is about a half of that of O_3w-S_1l (2.68 m^3/t).[5] Nevertheless, much more work has been devoted to the O_3w-S_1l. The pore characteristics of $\in_1$n shale reservoirs and corresponding influential factors remain uncertain, which may lead to misunderstanding of the resource potential of $\in_1$n gas shales.

In the current study, we investigated the characteristics of $\in_1$n shale reservoirs and analyzed the effects of various factors on the nanoscale pores. In addition to mineralogical and organic geochemical characterizations, low pressure N_2 adsorption and FE-SEM were employed to study the microscopic features of the pore systems. Based on our characterization results, this paper discusses the nanoscale characteristics of $\in_1$n shale from three aspects: sedimentary condition, shale composition, and thermal evolution.

2. EXPERIMENTAL DETAILS

2.1. Materials

A total of 14 black shale core samples were obtained from a well in the Kaiyang, Guizhou province. The samples were collected every a few meters from the top to the bottom of $\in_1$n. Figure 1 shows the sampling location and the regional geology. TOC content analysis, thermal maturity (R_o) tests, mineralogical composition analysis and low pressure N_2 adsorption were conducted on all of samples. Three samples (KY-3, KY-8, KY-13) were selected for FE-SEM imaging.

2.2. Organic Geochemical Analyses

A vario MACRO cube organic element analyzer was used to measure the TOC content of all samples following the Chinese Oil and Gas Industry Standard GB/T19145-2003. Before the measurement, inorganic carbon in the samples was eliminated with diluted hydrochloric acid with $HCl:H_2O = 1:7$ (V/V).

Because of the absence of vitrinite in the Lower Cambrian marine shale, the bitumen reflectance (R_b) was measured to reflect thermal maturity of samples. Laser Raman spectroscopy has been proved as a suitable method to calculate the bitumen reflectance.[34–36] A Renishaw Invia Reflex Laser Raman Spectrometer was used to measure the R_b values of all samples. Calculation of R_b in this paper follows the equation:[37] $R_b = 0.0537\ d\ (G - D) - 11.21$, where G, D, and d denote peak positions of the graphitic carbon and disordered carbon, and the inter-peak intervals ($G - D$), respectively. The relationship between R_b and R_o has been studied previously.[38–40] The following relation: $R_o = (R_b + 0.2443)/1.0495$, is used to calculate R_o.[40]

2.3. Mineralogical Composition

Mineralogical composition of samples was determined by a Panalytical Empyrean X-ray diffractometer (XRD) with the testing angle ranging from 5° to 80°. The samples were

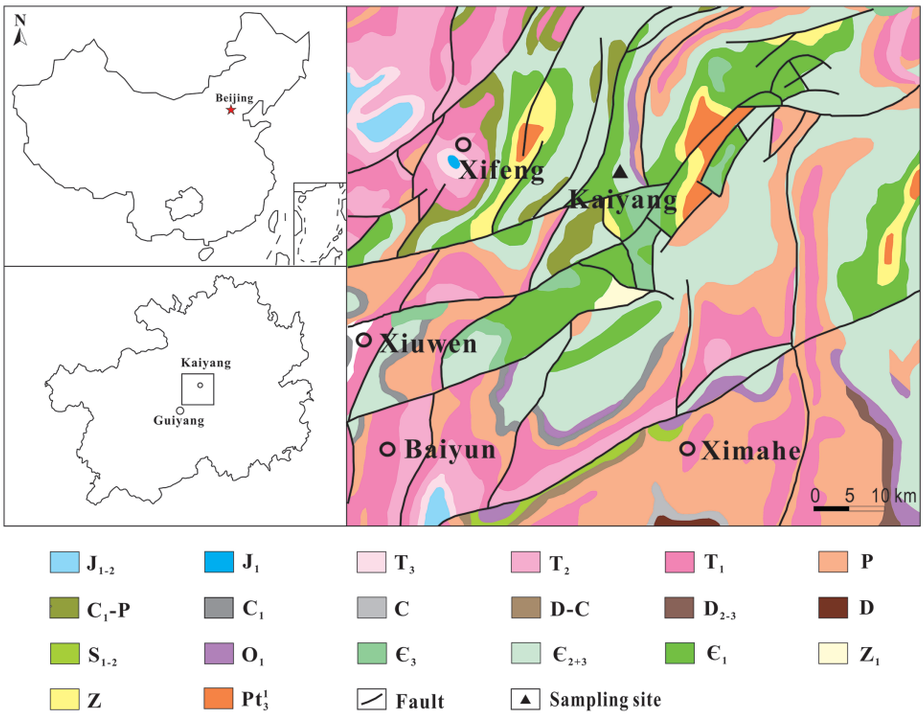

Figure 1. The sampling location and the regional geology.

crushed and then ground to 200 mesh, and the results were analyzed following the Chinese Oil and Gas Industry Standard (SY/T) 5163-2010.

2.4. Low Pressure N_2 Adsorption

Low pressure N_2 adsorption experiments were conducted on a Quantachrome autosorb-iQ_2 automatic gas absorption analyzer. All samples were ground to 80 mesh. In order to remove free water and volatile materials, the samples were outgassed at 150 °C for 4 hours before adsorption measurement. N_2 adsorption isotherms were obtained at 77 K (−196 °C) and the relative pressure (p/p_0) ranges from 10^{-6} to 0.99. The adsorption isotherms of the samples are presented in Figure 2. The specific surface area was calculated using multi-point Brunauer-Emmett-Teller (BET) method and total pore volume was converted from the adsorption data at the maximum p/p_0. Micropore volume and mesopore volume were acquired using density functional theory (DFT).

2.5. FE-SEM

Three samples (KY-3, KY-8, KY-13) were selected for FE-SEM. A smooth surface was first obtained through polishing the sample using a Technoorg SC1000 argon ion polisher operated at 8 kV acceleration voltage. Before SEM observation, a conductive surface was obtained through sputter-coating with gold. A FEI Scios FE-SEM operated at an acceleration voltage of 10 kV was used to characterize the surface morphology of the shale samples.

3. RESULTS AND DISCUSSION

3.1. Shale Composition and Sedimentary Environment

Burial depth, TOC content and R_o of 14 samples are presented in Table I. TOC content ranges from 0.74% to 5.83% with an average content of 3.35%. With the increase of burial depth, TOC content shows a significant increase. The R_o values (ranging from 2.39% to 3.29%) indicate that all samples are in the stage of over-maturation, and also increase with burial depth.

XRD was used to semi-quantitatively estimate the mineralogical composition of the 14 samples, and the results are presented in Table II. The dominant minerals of the samples are found to be quartz, clay minerals and plagioclase, while the minor minerals include pyrite, dolomite, calcite and so on. Quartz content varies from 38.1% to 57.1% with an average value of 47.3%. The content of clay minerals (illite, kaolinite, chlorite, etc.) ranges from 17.2% to 37.9% with an average value of 26.7%, which mainly consists of illite (average of 18.8%) and kaolinite (average of 6.4%). Plagioclase content varies from 0% to 32.0% with an average value of 18.4%. In addition, all samples contain a small amount of pyrite.

Shale composition is one of the assessment criteria of shale gas reservoirs,[41–44] and obviously has a serious impact on the resource potential of gas shales.[45,46] Sedimentary environment is an important control factor determining the shale composition.[10,31] Figure 3(a) reveals apparent positive correlations between burial depth, pyrite and TOC. In the FE-SEM images (Figs. 4(g), 5(e–h),

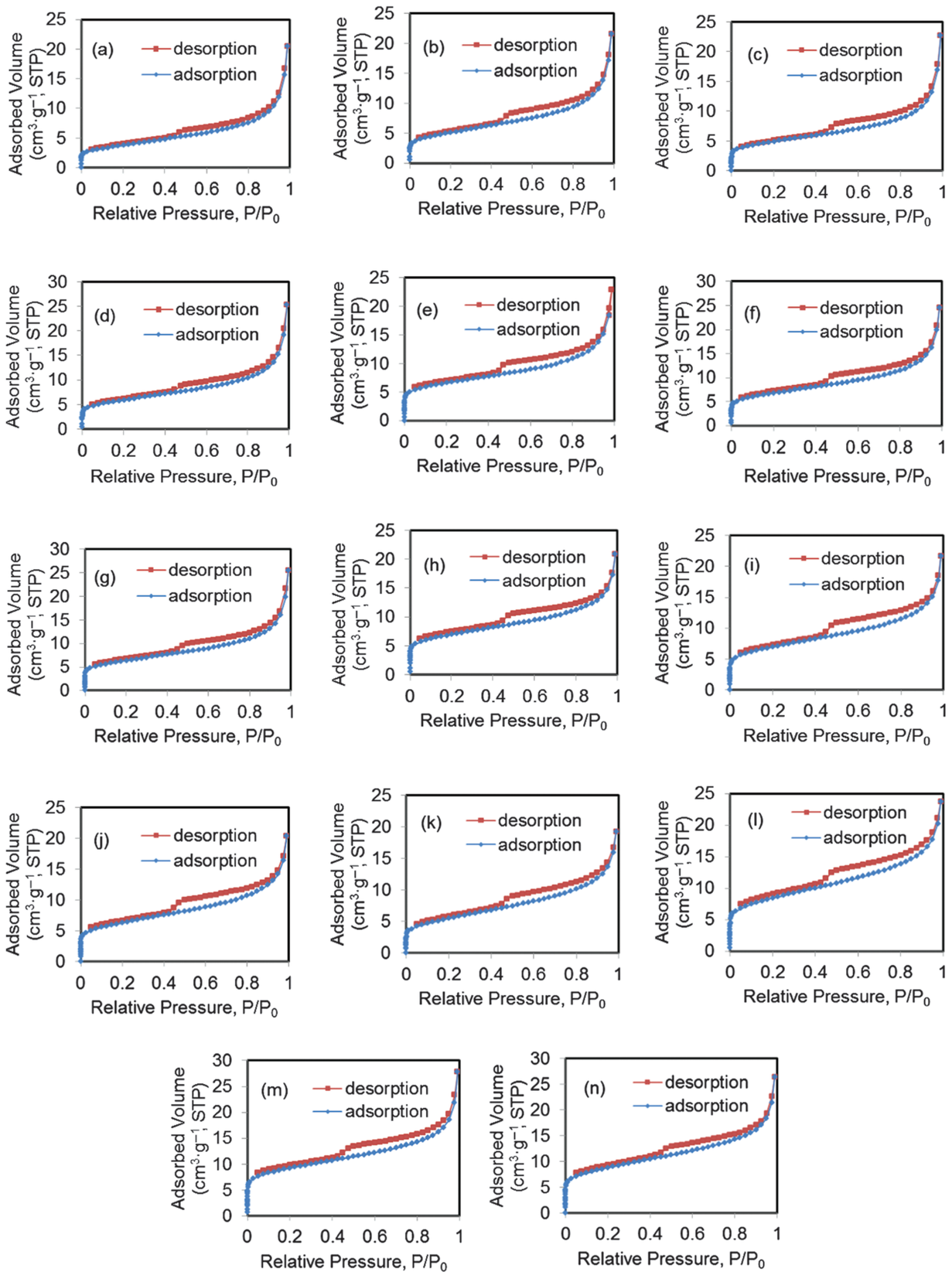

Figure 2. The adsorption–desorption isotherms of the 14 shale samples. (a–n) correspond to the samples KY-1 to KY-14, respectively.

Table I. Burial depth, TOC content and R_o of the 14 samples.

Sample ID	Burial Depth (m)	TOC (%)	R_b (%)	R_o (%)
KY-1	913.0	0.74	2.29	2.41
KY-2	920.7	1.56	2.26	2.39
KY-3	926.3	1.18	2.30	2.42
KY-4	932.8	1.64	2.36	2.48
KY-5	938.8	2.97	2.43	2.55
KY-6	942.0	2.82	2.43	2.55
KY-7	945.5	2.73	2.63	2.74
KY-8	948.0	4.76	2.49	2.61
KY-9	951.0	4.42	2.52	2.63
KY-10	954.4	4.00	2.79	2.89
KY-11	957.7	3.07	2.82	2.92
KY-12	961.0	5.83	3.25	3.23
KY-13	964.5	5.57	3.21	3.29
KY-14	967.5	5.57	3.05	3.14

6(c, g, h)), a considerable amount of pyrite crystals are easily found in close proximity to organic matter (OM), which is compatible with the positive correlation between TOC and pyrite. The occurrence of OM and pyrite is generally associated with an anoxic, reducing environment, and the correlations between burial depth, pyrite and TOC suggest that the lower strata were in a more reducing condition. The above results fit well with the epicontinental sea sedimentary environment of ϵ_1n in Guizhou province, with the lower ϵ_1n being deposited on a deep-water shelf and the upper on a shallow-water shelf.[47–50] Figure 3(b) shows a weak yet positive correlation between quartz and TOC, and a negative correlation between clay minerals and TOC. This heterogeneity in shale mineral composition may be because terrigenous clay minerals tend to deposit in shallow water and part of quartz in deep-water was biogenetic.[51] A higher content of quartz can increase the brittleness of shale, which is conducive to later reservoir reconstruction through hydraulic fracturing. It's observed that a combination of larger quartz and TOC contents in the lower ϵ_1n provides a favorable material basis for shale gas development.

Table II. Mineralogical composition of the 14 samples ("nd" = not detected).

Sample ID	Quartz (%)	Illite (%)	Kaolinite (%)	Plagioclase (%)	Pyrite (%)	Dolomite (%)	Calcite (%)	Chlorite (%)
KY-1	44.4	21.9	14.0	16.2	1.9	nd	1.6	nd
KY-2	47.8	20.6	11.8	15.3	1.6	1.2	1.7	nd
KY-3	44.4	17.3	13.0	16.1	1.9	nd	2.5	4.9
KY-4	45.3	21.4	9.4	13.9	1.8	1.1	nd	7.1
KY-5	50.0	18.4	6.7	17.4	2.4	4.2	1.1	nd
KY-6	49.0	22.8	4.5	13.2	2.6	6.6	1.4	nd
KY-7	49.9	26.4	nd	13.2	3.4	7.2	nd	nd
KY-8	45.3	13.4	nd	30.3	2.6	7.0	nd	3.8
KY-9	38.1	13.0	3.0	31.5	4.2	3.9	nd	6.4
KY-10	42.4	14.7	4.3	32.0	3.7	2.8	nd	nd
KY-11	40.9	15.7	2.9	31.7	3.1	5.8	nd	nd
KY-12	51.1	15.3	6.5	18.0	4.7	4.3	nd	nd
KY-13	56.5	18.5	5.4	8.6	3.7	6.6	nd	nd
KY-14	57.1	23.8	7.4	nd	4.0	7.8	nd	nd

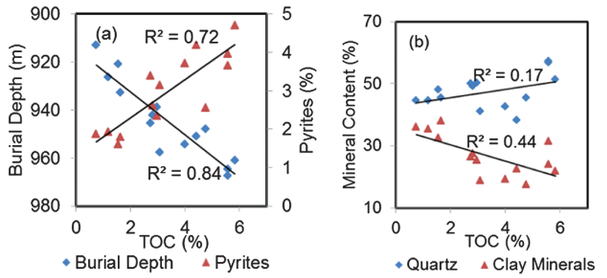

Figure 3. The relationships (a) between burial depth, pyrite and TOC, and (b) between quartz, clay minerals and TOC.

3.2. Pore Characteristics

3.2.1. Low Pressure N_2 Adsorption Characterization

Low pressure N_2 adsorption is one of the most common techniques to characterize nanoscale pore structures in shale gas reservoirs, as it can provide a reliable assessment of the surface area and pore size distribution. Figure 2 presents low pressure N_2 adsorption isotherms of 14 shale samples. All isotherms can be classified as Type IIb according to a refined International Union of Pure and Applied Chemistry (IUPAC) grouping method, and exhibit a similar Type H3 hysteresis loop.[52,53] Such an isotherm shape indicates that our samples contain all three pore types, i.e., micropores (<2 nm), mesopores (2–50 nm) and macropores (>50 nm).[53,54] The sharp increase of adsorption uptake at very low relative pressure ($p/p_0 < 0.01$) is most likely due to micropore filling. The monolayer-multilayer adsorption on the mesopore wall takes place at intermediate p/p_0, which is also responsible for the hysteresis. The existence of macropores results in the absence of the plateau (like in the mesoporous Type IV isotherms) and a steep slope in p/p_0 range of 0.98–1.00. According to IUPAC recommendations, the H3 type hysteresis loops in our shale samples indicate the presence of slit-shaped pores.[52]

Pore structure parameters including specific surface area, pore volume, etc., are given in Table III. The BET specific surface area, ranging from 13.4 m^2/g to 32.8 m^2/g with a mean value of 23.1 m^2/g, shows an obvious rising trend with burial depth. Total pore volume varies from 0.030 cm^3/g to 0.043 cm^3/g with a mean value of 0.036 cm^3/g. It is important to note that the mesopore volume accounts for 60–70% of the total pore volume in all our samples, while the micropore volume accounts for 4–16% of the total pore volume. The average pore diameter (4.9–9.4 nm) also falls in the mesopore range. Clearly, mesopore is the dominant pore component in the ϵ_1n shale samples.

3.2.2. FE-SEM Observation

The complex structure of nanoscale pores plays an critical role in controlling the storage and migration of hydrocarbons in the shale gas reservoirs.[29] While low

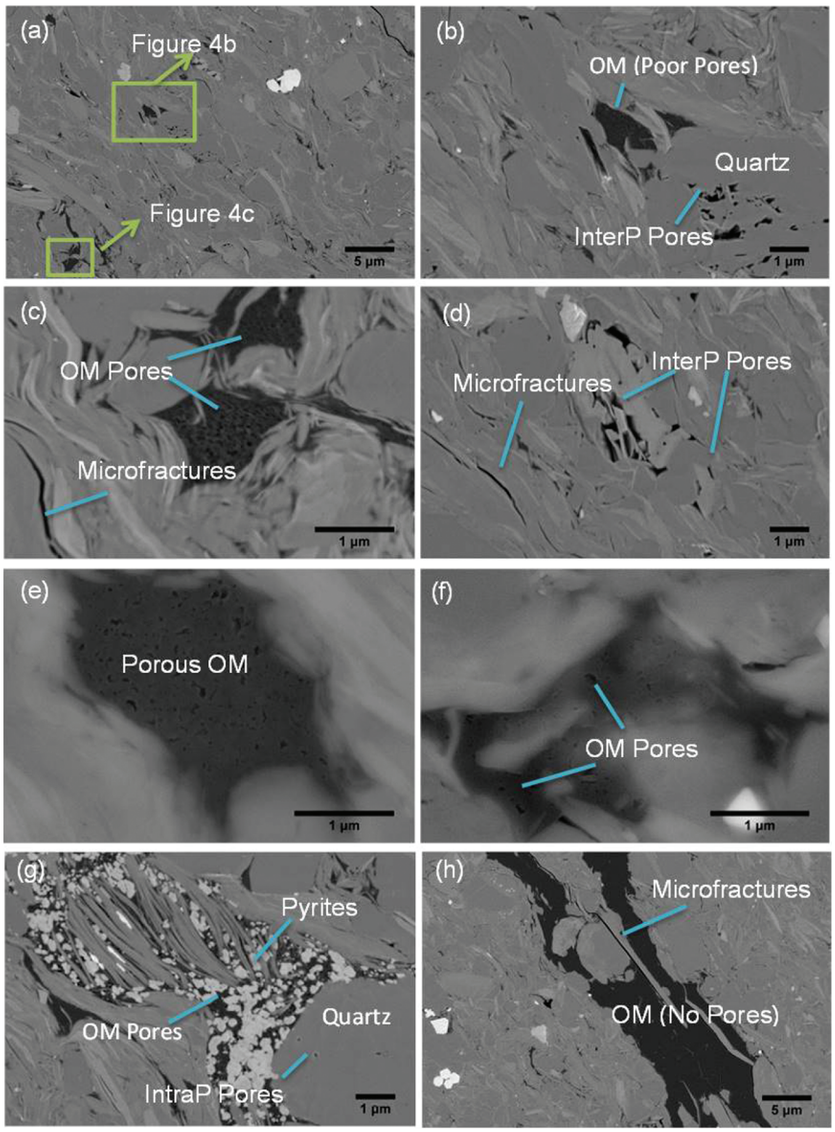

Figure 4. FE-SEM images for sample KY-3. (a) Overview in large range of sample KY-3; (b–c) magnification of the rectangle shown in (a, b) OM with poor pores and interP pores of quartz, (c) OM pores in single OM grain and microfractures; (d) InterP pores of minerals and microfractures; (e–f) OM pores with irregular and elliptical shape; (g) OM pores within the OM combined with pyrites and intraP pores in quartz; (h) OM with no pores and microfractures.

pressure N_2 adsorption is particularly useful in providing a comprehensive statistical description of the pore characteristics, electron microscopy is unique in enabling direct, high-magnification observation of the pore structures. To observe and analyze morphological characteristics of nanopores in $\in_1$n shale, FE-SEM was used to characterize three representative samples (KY-3, KY-8, KY-13) having different burial depth and TOC. Consistent with previous studies, pores in our shale samples can be classified into OM pores (pores within organic matter), interP pores (pores between particles or crystals), intraP pores (pores within particles) and microfractures.[13, 21, 22] The images of the sample KY-3 are presented in Figure 4. It is found that OM pores (c, e, f) and interP pores (b, d) were developed very well, while intraP pores (g) were less developed. The size of interP pores is generally greater than that of OM pores and intraP pores. Moreover, microfractures (c, d, h) between minerals were also developed well, which could be very important for the storage and permeable migration of shale gas.[13, 22, 55] Figure 5 presents a variety of pores in sample KY-8, including OM pores (a–c, g, h), intercrystalline pores within pyrite framboids (g, h), intraP pores (f) in quartz and pores in OM-clay aggregates (b, d, e–f). It appears

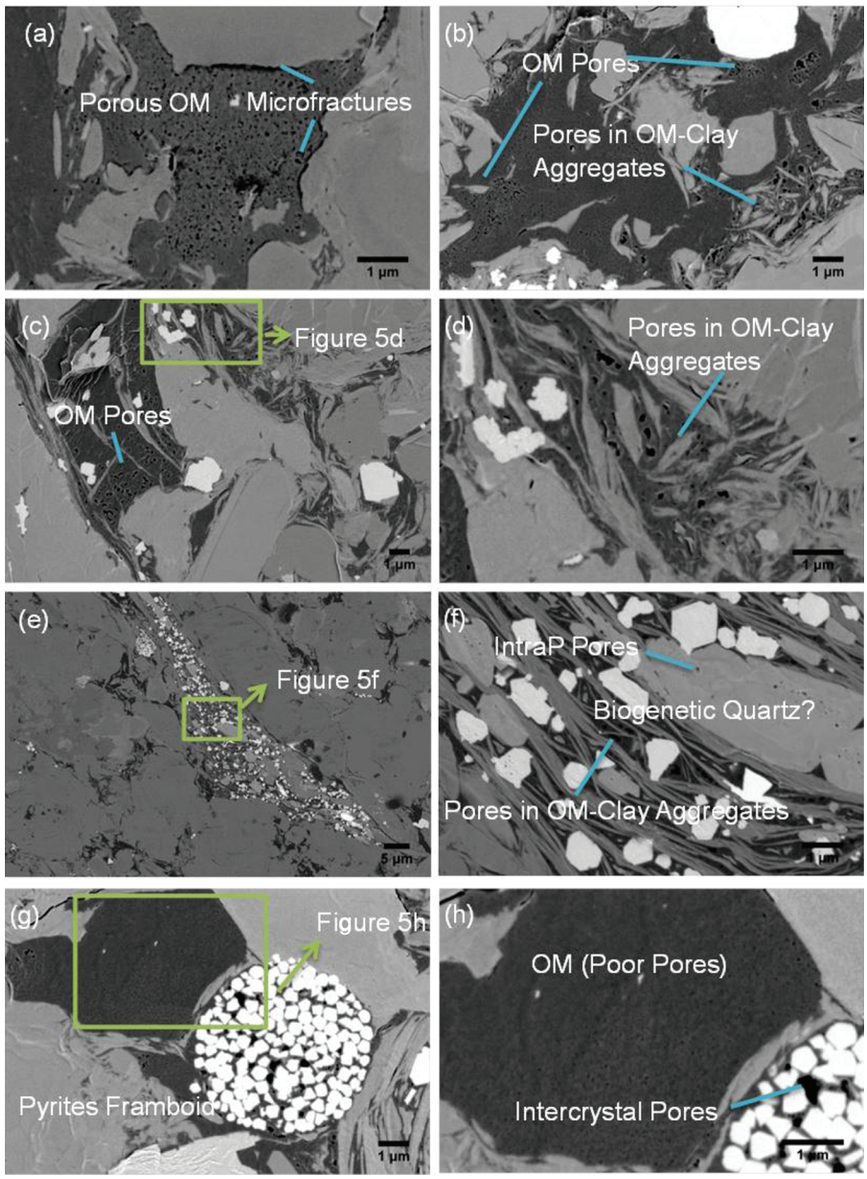

Figure 5. FE-SEM images for sample KY-8. (a–c) Porous OM; (b–f) pores in OM-clay aggregates; (g–h) OM with poor pores and intercrystal pores in pyrites framboid.

that more OM pores were developed in sample KY-8 than in sample KY-3, which may be related to the increase of TOC content and thermal maturity in KY-8.[56, 57] Considerable OM-clay aggregates with nanoscale pores are found in Figure 5, where the aggregates do not seem to have any preferred orientational arrangement. In sample KY-13 (Fig. 6), it is more difficult to find OM pores (a–d) than in samples KY-3 and KY-8. However, pores in OM-clay aggregates (c–h) seem to be more easily identified in KY-13. Meanwhile, OM-clay aggregates in sample KY-13 are almost parallel to bedding, which is very different from sample KY-8 and may be caused by stratum pressure.

3.3. The Influential Factors of Pore Characteristics

3.3.1. Effect of Organic Matter

Figure 7 presents the relationship between pore structure parameters and TOC content. Similar to previous studies,[20, 48, 58, 59] the specific surface area and micropore volume show positive correlations with TOC content (correlation coefficient of 0.85 and 0.79, respectively), while the total pore volume and mesopore volume are slightly correlated with TOC content. The above correlational analysis indicates that organic matter makes a significant contribution to both specific surface area and micropore volume, which is also compatible with the geometric fact that micropore contributes more surface area than meso- or

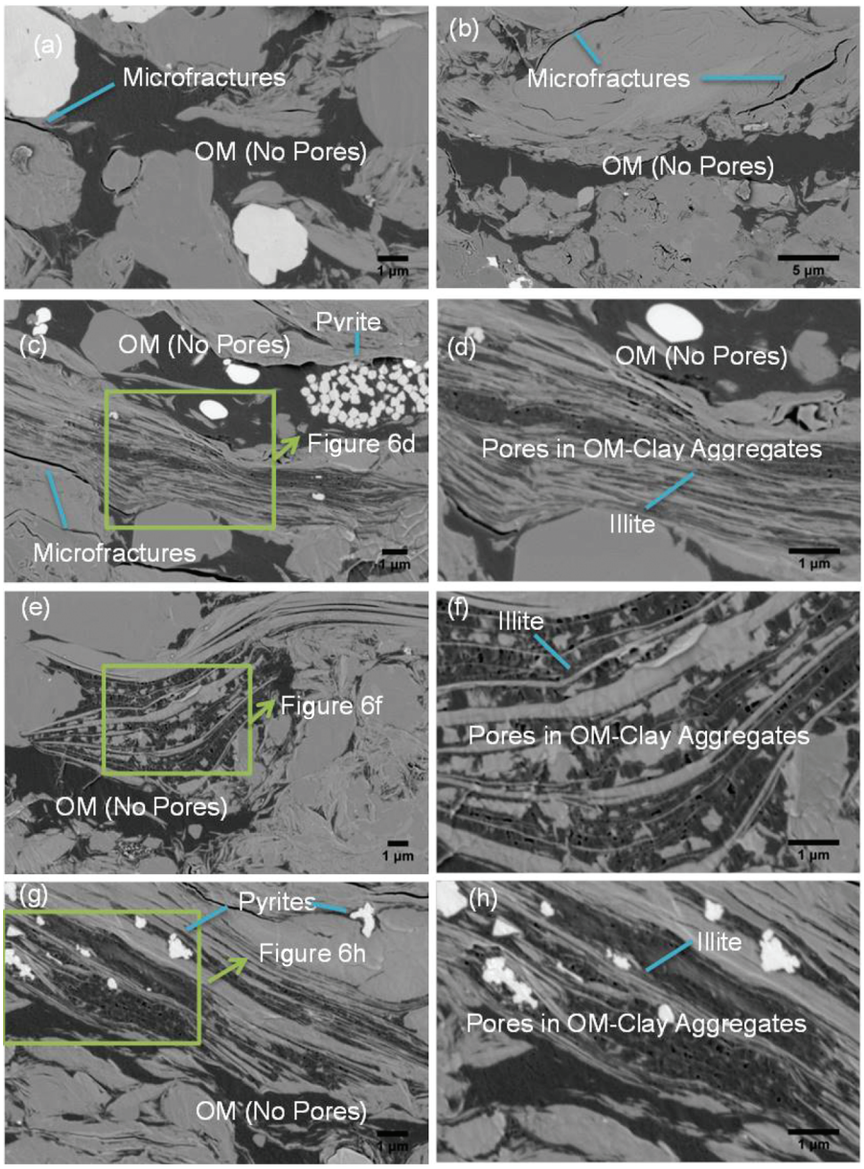

Figure 6. FE-SEM images for sample KY-13. (a–b) OM with no pores and microfractures; (c–h) pores in OM-clay aggregates.

macropore when the pore volume is the same. The positive correlation between TOC content and specific surface area is also consistent with a recent study indicating that higher TOC content promoted methane sorption in the shale.[60] In addition, with the increase of TOC content, the average pore diameter decreases at first and then becomes nearly steady at the higher TOC end (Fig. 7), which is similar to the results of an earlier study on Permian shale.[61] The negative correlation between the average pore size and TOC may be caused by two reasons: first, micropores tend to exist in organic matter, which results in a smaller overall pore size at higher TOC; secondly, both TOC content and stratum pressure increase with burial depth, which leads to more severe compaction of pores (especially OM pores) in the later diagenesis.

3.3.2. *Effect of Minerals*

The relationship between pore structure parameters and quartz is illustrated in Figure 8. Total pore volume and mesopore volume apparently show better positive correlations with quartz than specific surface area and micropore volume. The SEM images of samples KY-3 and KY-8 (Figs. 4(b, g); 5(f)) reveal a lot of mesopores and macropores within quartz, which is consistent with the better correlation between pore volume and quartz. Since smaller pores are much harder to observe, poor identification of micropores from SEM images cannot be used as an evidence to deny the ability of quartz (same as OM) to generate pores less than 2 nm. However, the positive correlations of specific surface area and micropore volume with quartz may be partly attributed to a weak positive

Table III. Pore structure parameters of the 14 samples.

Sample ID	Specific Surface Area (BET) (m^2/g)	Total Pore Volume (cm^3/g)	Micropore Volume (DFT) (cm^3/g)	Mesopore Volume (DFT) (cm^3/g)	Average Pore Diameter (nm)
KY-1	13.4	0.032	0.0012	0.022	9.4
KY-2	18.1	0.033	0.0023	0.023	7.4
KY-3	17.4	0.035	0.0026	0.022	8.1
KY-4	20.8	0.039	0.0034	0.025	7.5
KY-5	23.3	0.036	0.0044	0.023	6.1
KY-6	23.9	0.038	0.0041	0.025	6.3
KY-7	22.4	0.039	0.0036	0.026	7.0
KY-8	24.7	0.032	0.0048	0.021	5.2
KY-9	24.7	0.033	0.0044	0.022	5.4
KY-10	22.3	0.032	0.0037	0.021	5.7
KY-11	19.4	0.030	0.0024	0.021	6.1
KY-12	29.7	0.037	0.0054	0.025	4.9
KY-13	32.8	0.043	0.0068	0.026	5.2
KY-14	31.1	0.041	0.0056	0.026	5.3

correlation (Fig. 3(b)) between TOC and quartz. No significant relationship was found between quartz and average pore diameter.

The influences of illite content on the pore structure parameters are shown in Figure 9. Specific surface area and micropore volume exhibit no apparent correlations with illite content. However, total pore volume and mesopore volume display moderate positive correlations with illite content, which indicates some mesopores and macropores may be controlled by illite. Accordingly, a number of mesopores and macropores are found in illite or OM-clay aggregates from the SEM images of our samples (Figs. 5(b, d, f); 6(c–h)). A weak positive relationship is also found between average pore diameter and illite content.

3.3.3. *Effect of Thermal Evolution*

When sediments are buried and subjected to increased temperature and pressure, organic matter passes through three stages of thermal maturation: diagenesis, catagenesis and metagenesis (Fig. 10).[62] In the stage of diagenesis, which occurs in shallow sub-surface and begins during initial deposition and burial, organic matter is converted into kerogen and possibly generates biogenic methane. The catagenesis stage happens in deeper sub-surface at higher stratum pressure and temperature, which leads to generation of large amounts of hydrocarbons (oil and gas). Metagenesis is the last stage of the thermal evolution process, in which dry gas is generated by the transformation of remaining kerogen and heavier hydrocarbons. $\in_1$n shale most likely has passed through all three phases of organic matter transformation and consequently organic matter is over-matured. Generation of large amounts of hydrocarbons in the catagenesis stage and the early stage

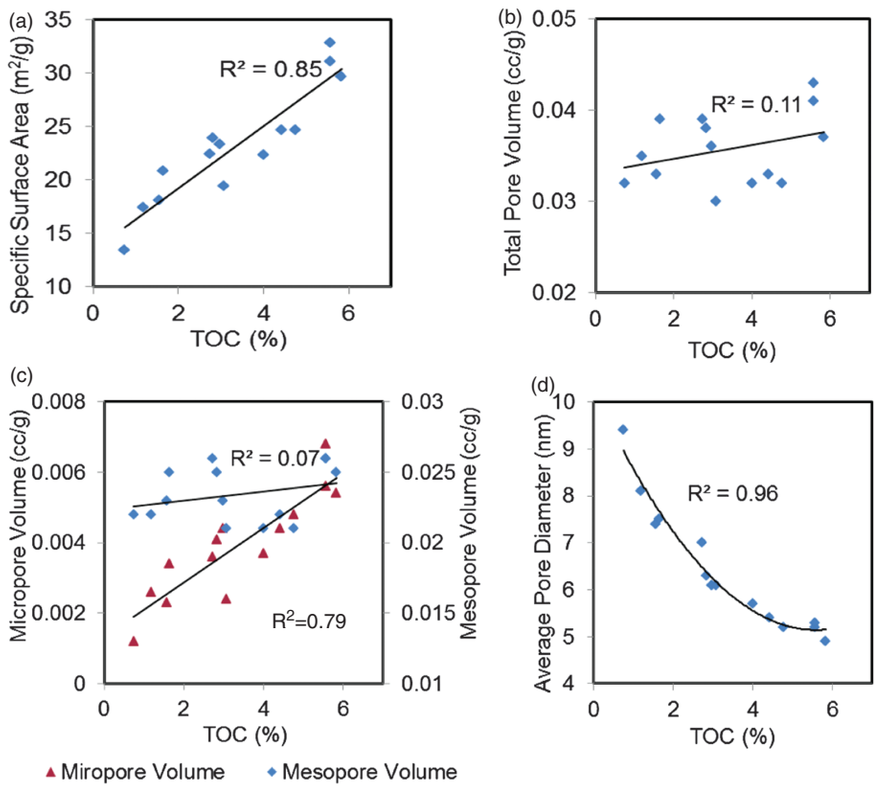

Figure 7. The relationships (a) between specific surface area and TOC content; (b) between total pore volume and TOC content; (c) between micropore volume, mesopore volume and TOC content; (d) between average pore diameter and TOC content.

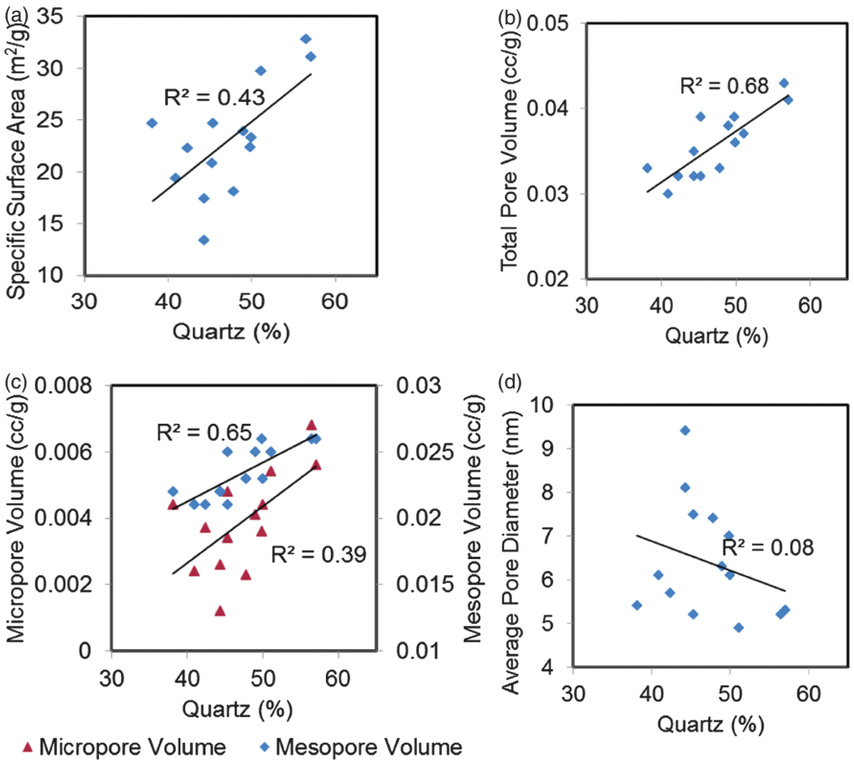

Figure 8. The relationships (a) between specific surface area and quartz; (b) between total pore volume and quartz; (c) between micropore volume, mesopore volume and quartz; (d) between average pore diameter and quartz.

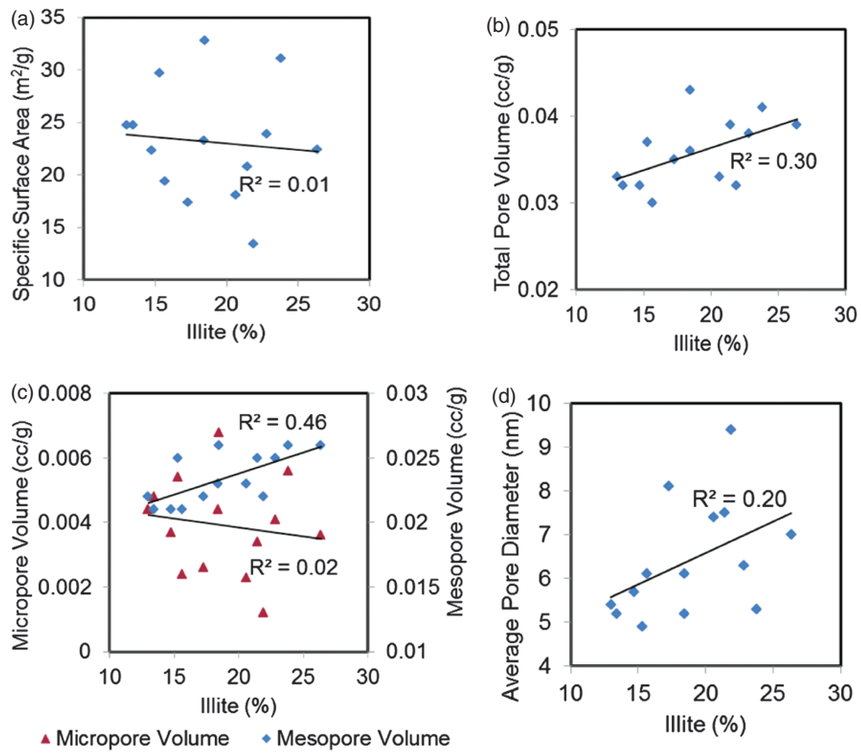

Figure 9. The relationships (a) between specific surface area and illite; (b) between total pore volume and illite; (c) between micropore volume, mesopore volume and illite; (d) between average pore diameter and illite.

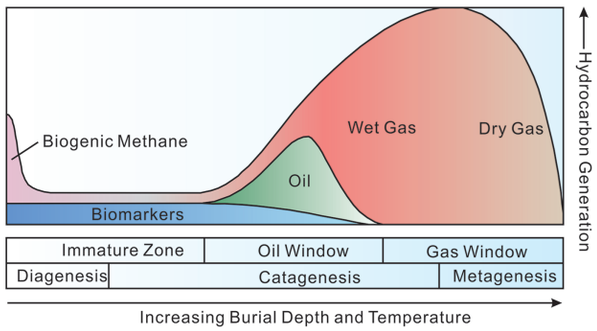

Figure 10. The maturation stages in the process of hydrocarbon generation (modified after Alexander et al.).[62]

of metagenesis resulted in the development of OM pores and possibly formation of overpressure.[63] Subsequently, due to multi-period tectonic movements, shale reservoir developed lots of fractures,[55] which could cause significant dissipation of hydrocarbons. Then, it is very possible that pores in the over-matured OM (more brittle) could not stand the stratum pressure and became severely compacted.[8, 64] The combined action of gas dissipation and pore compaction may explain the observation of less development or smaller size of OM pores at larger burial depth (compare OM pores in Figs. 5 and 6).

As discussed earlier, clay minerals tend to deposit more in shallow water. In deep-water, however, clay minerals should deposit more slowly. Combined with higher pressure, clay layers at larger burial depths could adopt an orientational arrangement parallel to the seabed (see Fig. 6). After deposition, along with increasing thermal maturity and burial depth of shale, smectite may gradually transform into illite, and organic matter can be adsorbed on the illite surface forming OM-clay aggregates parallel to the bedding of shale (Fig. 6).[65, 66] Because of the protection of illite layers, hydrocarbons in OM-clay aggregate pores may be harder to migrate out, which could help maintain an over-pressure and prevent pores in OM-clay aggregates from being compacted by stratum pressure (Fig. 6). We speculate that these pores may be the main storage space of shale gas in the bottom of ϵ_1n. Because of the protection of clay minerals, ordinary hydraulic fracturing techniques may not guarantee efficient access to the pores in OM-clay aggregates, which is likely to be one of the reasons for the unsuccessful exploitation of ϵ_1n shales.[67] On the other hand, innovation of hydraulic fracturing toward improving access to the pores in OM-clay aggregates may hold promise for enhancing the efficiency in the exploration and production of ϵ_1n shale gas reservoirs.

4. CONCLUSIONS

Focusing on nanoscale pore characteristics, we have systematically studied the variation of reservoir composition and structure over burial depth using 14 shale core samples from the Lower Cambrian Niutitang formation in Guizhou province. The apparent trend in our samples of increasing TOC content and decreasing clay content with burial depth seems quite compatible with the epicontinental sea sedimentary environment of ϵ_1n in Guizhou. N_2 adsorption indicates that our ϵ_1n samples contain all three pore types in terms of pore size classification (i.e., micropores, mesopores and macropores), with mesopores contributing to 60–70% of the total pore volume. Morphological observations confirm the existence of OM pores, interP pores, intraP pores and microfractures. It is highly possible that micropores are dominantly generated by OM, and accordingly OM significantly contributes to the specific surface area. In contrast, mesopores should be mostly contributed by illite and quartz. The rapid decrease of average pore size appears to be closely associated with the OM content.

OM pores are generated during the transformation of OM into hydrocarbons, and are important storage space for shale gas. It is found that OM pores were abundantly developed in the middle-upper of ϵ_1n shale, but less well in the bottom of ϵ_1n. However, considerable OM-clay aggregates preferentially parallel to the shale bedding were found in the bottom of ϵ_1n, which developed significant amount of nanoscale pores. The vertical difference in the pore distribution may be attributed to several factors, including sedimentary condition, long-term OM thermal maturation, tectonic movements, compaction due to stratum pressure, and possibly protection (from compaction) provided by clay minerals. Although the lower ϵ_1n exhibits favorable qualities as promising shale gas reservoirs, current challenges on the exploitation of ϵ_1n shales remain formidable. Undoubtedly, further research on the reservoir properties and corresponding exploration and fracturing techniques are necessary in order to better understand the resource potential of ϵ_1n gas shales. In our opinion, future success on the development of ϵ_1n gas shales should rely not only on locating the sweet spot where the gas preservation conditions are optimal, but also on the innovation of hydraulic fracturing toward improved accessibility of all types of pore spaces with a special focus on the OM-clay aggregate pores, which may be the main storage space of shale gas in the bottom of ϵ_1n.

Acknowledgment: This work is supported by the Chinese Academy of Sciences ("Hundred Talents Program"), the National Natural Science Foundation of China (41473064), and the State Key Laboratory of Ore Deposit Geochemistry (SKLODG-ZY125-09).

References and Notes

1. G. R. Chalmers, R. M. Bustin, and I. M. Power, *AAPG Bulletin* 96, 1099 (**2012**).
2. J. B. Curtis, *AAPG Bulletin* 86, 1921 (**2002**).
3. C. N. Zou, D. Z. Dong, S. J. Wang, J. Z. Li, X. J. Li, Y. M. Wang, D. H. Li, and K. M. Cheng, *Petroleum Exploration and Development* 37, 641 (**2010**).

4. D. W. Zhang, Y. X. Li, J. C. Zhang, D. W. Qiao, W. L. Jiang, and J. F. Zhang, Resource Potential Evaluation of Shale Gas in China, Geological Publishing House, Beijing **(2012)**.
5. D. Z. Dong, Y. M. Wang, X. J. Li, C. N. Zou, Q. Z. Guan, C. C. Zhang, J. L. Huang, S. F. Wang, H. Y. Wang, H. L. Liu, W. H. Bai, F. Liang, W. Lin, Q. Zhao, D. X. Liu, and Z. Qiu, *Natural Gas Industry* 36, 19 **(2016)**.
6. W. F. Fan, D. J. Hou, and Y. Liang, *Science Technology and Engineering* 15, 13 **(2015)**.
7. Z. G. Wang, *Oil and Gas Geology* 36, 1 **(2015)**.
8. H. Tian, L. Pan, T. W. Zhang, X. M. Xiao, Z. P. Meng, and B. J. Huang, *Marine and Petroleum Geology* 62, 28 **(2015)**.
9. L. Zhao, Y. Z. He, P. Yang, H. G. Chen, and Y. Y. An, *Geology of China* 42, 1931 **(2015)**.
10. S. Bernard and B. Horsfield, *Annual Review of Earth and Planetary Sciences* 42, 635 **(2014)**.
11. R. G. Loucks, R. M. Reed, S. C. Ruppel, and D. M. Jarvie, *Journal of Sedimentary Research* 79, 848 **(2009)**.
12. M. E. Curtis, C. H. Sondergeld, R. J. Ambrose, and C. S. Rai, *AAPG Bulletin* 96, 665 **(2012)**.
13. R. M. Slatt and N. R. O'Brien, *AAPG Bulletin* 95, 2017 **(2011)**.
14. P. H. Nelson, *AAPG Bulletin* 93, 329 **(2009)**.
15. S. B. Chen, Y. M. Zhu, H. Y. Wang, H. L. Liu, W. Wei, and J. H. Fang, *Journal of China Coal Society* 37, 438 **(2012)**.
16. C. R. Clarkson, N. Solano, R. M. Bustin, A. M. M. Bustin, G. R. L. Chalmers, L. He, Y. B. Melnichenko, A. P. Radliński, and T. P. Blach, *Fuel* 103, 606 **(2013)**.
17. M. Mastalerz, L. He, Y. B. Melnichenko, and J. A. Rupp, *Energy and Fuels* 26, 5109 **(2012)**.
18. G. C. Wang, Y. W. Ju, Z. F. Yan, and Q. G. Li, *Marine and Petroleum Geology* 62, 1 **(2015)**.
19. C. N. Zou, R. K. Zhu, B. Bai, Z. Yang, S. T. Wu, L. Su, D. Z. Dong, and X. J. Li, *Acta Petrologica Sinica* 27, 1857 **(2011)**.
20. Y. Wang, Y. M. Zhu, S. B. Chen, and W. Li, *Energy and Fuels* 28, 945 **(2014)**.
21. R. G. Loucks, R. M. Reed, S. C. Ruppel, and U. Hammes, *AAPG Bulletin* 96, 1071 **(2012)**.
22. F. Yang, Z. F. Ning, Q. Wang, and H. Q. Liu, *Marine and Petroleum Geology* 70, 14 **(2016)**.
23. Y. Ma, N. N. Zhong, X. Y. Huang, Z. P. Guo, and L. P. Yao, *Journal of Chinese Electron Microscopy Society* 33, 251 **(2014)**.
24. A. M. M. Bustin and R. M. Bustin, *International Journal of Coal Geology* 103, 132 **(2012)**.
25. R. C. Hartman, R. J. Ambrose, I. Y. Akkutlu, and C. R. Clarkson, *Paper SPE 144097 Presented at the SPE Unconventional Gas Conference Held in the Woodlands*, Texas, June **(2011)**.
26. F. Yang, Z. F. Ning, S. D. Zhang, C. P. Hu, L. H. Du, and H. Q. Liu, *Natural Gas Industry* 33, 135 **(2013)**.
27. A. P. Ranlinski, C. J. Boreham, G. D. Wignall, and J. S. Lin, *Physical Review* 53, 14152 **(1996)**.
28. E. Vergés, D. Tost, D. Ayala, E. Ramos, and S. Grau, *Sedimentary Geology* 234, 109 **(2011)**.
29. X. Gu, D. R. Cole, G. Rother, D. F. R. Mildner, and S. L. Brantley, *Energy and Fuels* 29, 1295 **(2015)**.
30. X. M. Cao, B. S. Yu, X. T. Li, M. D. Sun, and L. Zhang, *Acta Petrolei Sinica* 35, 233 **(2014)**.
31. X. D. Fu, J. Z. Qin, and G. Teng, *Petroleum Exploration and Development* 38, 671 **(2011)**.
32. M. Y. Hu, Q. J. Deng, and X. S. Qiu, *Journal of Oil and Gas Technology* 35, 1 **(2013)**.
33. Y. Wu, T. L. Fan, S. Jiang, X. Q. Yang, H. Y. Ding, M. M. Meng, and D. Wei, *Energy and Fuels* 29, 4160 **(2015)**.
34. T. David, *Spectroscopy* 28, 20 **(2013)**.
35. S. R. Kelemen and H. L. Fang, *Energy and Fuels* 15, 653 **(2001)**.
36. S. B. Chen, Z. X. Zuo, Y. M. Zhu, C. Q. Fu, and H. Zhang, *Natural Gas Geoscience* 26, 564 **(2015)**.
37. D. H. Liu, X. M. Xiao, H. Tian, Y. S. Min, Q. Zhou, P. Cheng, and J. G. Shen, *Chinese Science Bulletin* 58, 1285 **(2012)**.
38. D. H. Liu and J. Y. Shi, *Petroleum Exploration and Development* 21, 113 **(1994)**.
39. G. X. Feng and S. J. Chen, *Natural Gas Industry* 8, 20 **(1988)**.
40. J. Schoenherr, R. Littke, J. L. Urai, P. A. Kukla, and Z. Rawahi, *Organic Geochemistry* 38, 1293 **(2007)**.
41. F. J. Jiang, X. Q. Pang, X. C. Ouyang, J. G. Guo, and C. Jin, *Earth Science Frontiers* 19, 198 **(2012)**.
42. Y. Q. Jiang, D. Z. Dong, L. Qi, Y. F. Shen, C. Jiang, and P. W. He, *Natural Gas Industry* 30, 7 **(2010)**.
43. Y. X. Li, D. W. Qiao, W. L. Jiang, and C. H. Zhang, *Geological Bulletin of China* 30, 308 **(2011)**.
44. Y. Tu, H. Y. Zou, H. P. Meng, Z. Y. Xia, and N. Li, *Oil and Gas Geology* 35, 153 **(2014)**.
45. D. J. K. Ross and R. Marc Bustin, *Marine and Petroleum Geology* 26, 916 **(2009)**.
46. J. J. Li, X. T. Yan, W. M. Wang, Y. N. Zhang, J. X. Yin, S. F. Lu, F. W. Chen, Y. L. Meng, X. W. Zhang, X. Chen, Y. X. Yan, and J. X. Zhu, *Applied Geochemistry* 58, 88 **(2015)**.
47. Y. N. Lu, J. C. Zhang, P. Zhang, Y. Q. Huang, F. F. Yu, and E. D. Deng, *Marine Origin Petroleum Geology* 20, 37 **(2015)**.
48. C. Luo, S. G. Liu, Z. L. Luo, W. Sun, B. Ran, S. Y. Wang, D. Yang, Z. Q. Bai, Y. H. Ye, X. Zhang, and B. Deng, *Geological Science and Techology Information* 33, 93 **(2014)**.
49. P. Yang, Z. J. Wang, Y. Xie, Q. D. Du, H. G. Chen, and Y. Z. He, *Geological Bulletin of China* 31, 1901 **(2012)**.
50. J. P. Zhang, T. L. Fan, J. C. Zhang, Y. F. Li, and Y. Wu, *Geoscience* 27, 978 **(2013)**.
51. C. J. Wu, M. F. Zhang, W. Y. Ma, Y. Liu, D. M. Xiong, L. N. Sun, and J. C. Tuo, *Natural Gas Geoscience* 25, 1267 **(2014)**.
52. K. S. W. Sing, D. H. Everett, R. A. M. Haul, L. Moscou, R. A. Pierotti, J. Rouquerol, and T. Siemeiniewska, *Pure and Applied Chemistry* 57, 1 **(1985)**.
53. F. Rouquerol, J. Rouquerol, and K. Sing, Adsortion by Powders and Porous Solids, Academic Press, San Diego **(1999)**.
54. J. Rouquerol, D. Avnir, C. W. Fairbridge, and D. H. Everett, *Pure and Applied Chemistry* 66, 1739 **(1994)**.
55. W. T. Zeng, J. C. Zhang, W. L. Ding, S. Zhao, Y. Q. Zhang, Z. J. Liu, and K. Jiu, *Journal of Asian Earth Sciences* 75, 251 **(2013)**.
56. J. Chen and X. M. Xiao, *Fuel* 129, 173 **(2014)**.
57. M. E. Curtis, B. J. Cardott, C. H. Sondergeld, and C. S. Rai, *International Journal of Coal Geology* 103, 26 **(2012)**.
58. H. L. Bu, Y. W. Ju, J. Q. Tan, G. C. Wang, and X. S. Li, *Journal of Natural Gas Science and Engineering* 24, 166 **(2015)**.
59. R. Yang, S. He, J. Z. Yi, and Q. H. Hu, *Marine and Petroleum Geology* 70, 27 **(2016)**.
60. J. Q. Tan, P. Weniger, B. Krooss, A. Merkel, B. Horsfield, J. C. Zhang, C. J. Boreham, G. Graas, and B. A. Tocher, *Fuel* 129, 204 **(2014)**.
61. L. Pan, X. M. Xiao, H. Tian, Q. Zhou, J. Chen, T. F. Li, and Q. Wei, *International Journal of Coal Geology* 146, 68 **(2015)**.
62. T. Alexander, J. Baihly, C. Boyer, B. Clark, and G. Waters, *Oilfield Review* 23, 40 **(2011)**.
63. H. L. Liu, H. Y. Wang, C. H. Fang, W. Guo, and S. S. Sun, *Earth Science Frontiers* 23, 48 **(2016)**.
64. U. Kuila and M. Prasad, *Geophysical Prospecting* 61, 341 **(2013)**.
65. L. F. Lu, J. G. Cai, W. H. Liu, Tenger, and J. Wang, *Oil and Gas Geology* 34, 16 **(2013)**.
66. M. J. Kennedy, S. C. Löhr, S. A. Fraser, and E. T. Baruch, *Earth and Planetary Science Letters* 388, 59 **(2014)**.
67. Y. W. Ju, H. L. Bu, and G. C. Wang, *Advance in Earth Sciences* 29, 492 **(2014)**.

Received: 12 March 2016. Accepted: 1 October 2016.